Journal of Ocean Engineering and Marine Energy
https://doi.org/10.1007/s40722-025-00384-y

CASE STUDY

Benchmark study of the DTU OWC chamber with both two-way and one-way absorption

Harry B. Bingham[1] · Bárður Joensen[1,2] · Robert W. Read[1] · Kim Nielsen[3,4] · Thanh Toan Tran[5] · Hafiz Ahsan Said[6] · Thomas Kelly[7] · John V. Ringwood[6] · Yasutaka Imai[8] · Joep van der Zanden[9] · Yi-Hsiang Yu[10] · Claes Eskilsson[4,11] · Alex Abolfazl Shiri[11]

Received: 31 May 2024 / Accepted: 7 February 2025

Abstract

This paper reports on a benchmark study based on small-scale (1:50) measurements of a single, oscillating water column chamber mounted sideways in a long flume. The geometry of the OWC chamber is extracted from a barge-like, attenuator-type floating concept "KNSwing" with 40 chambers targeted for deployment in the Danish part of the North Sea. In addition to traditional two-way energy extraction we also consider one-way energy extraction with passive venting and compare chamber response, pressures and total absorbed energy between the two methods. A blind study was established for the numerical modeling, with participants applying several implementations of weakly nonlinear potential flow theory and commercial Navier–Stokes solvers (CFD). Both compressible and incompressible models were used for the air phase. Potential flow calculations predict more energy absorption near the chamber resonance for one-way absorption than for two-way absorption, but the opposite is found from the experimental measurements. This outcome is mainly attributed to energy losses in the experimental passive valve system, but this conclusion must be confirmed by better experimental measurements. Modeling the one-way valve in CFD proved to be very challenging and only one team was able to provide results which were generally closer to the experiments. The study illustrates the challenges associated with both numerical and experimental analysis of OWC chambers. Air compressibility effects were not found to be important at this scale, even with the large volume of additional air used for the one-way case.

Keywords Wave energy · Oscillating water columns · Experimental measurements · Numerical models · Benchmark study

1 Introduction

The International Energy Agency Technology Collaboration Programme for Ocean Energy Systems (OES) IEA (2022) has been working since 2001 to promote guidelines for the commercialization of wave energy converters (WECs). The initiative currently includes 25 member countries from around the world. In 2016, the OES Task 10 on numerical modeling and verification of WEC systems was approved to assess the accuracy and reliability of numerical models for all aspects of WEC development. Initial results and conclusions were reported in Wendt et al. (2019) for two single degree-of-freedom point absorbers. This was followed by a study of a breakwater-mounted oscillating water column (OWC) device tested at large scale (1:4) and reported in Bingham et al. (2021). In parallel, a set of highly accurate decay test experiments on a floating sphere was presented by Kramer et al. (2021), providing benchmark results with small enough uncertainties to definitively quantify the accuracy of different numerical models.

In this paper, we report on the next stage of this work which considers the response of a single fixed OWC chamber using both two-way and one-way energy capturing strategies. In a traditional OWC chamber, the turbine is either a Wells type or a self-rectifying impulse or bi-radial turbine which extracts energy on both the up- and down-stroke of the chamber oscillation. An alternative strategy is to install a passive or active release valve in the chamber allowing the water to flow in or out freely on one half of the cycle. The valve then closes and air is forced through the turbine in only one direction on the other half-cycle. Although not intuitively obvious, it is possible to extract the same (or even more) total mechanical energy using a one-way strategy. The one-way strategy also allows for the installation of a one-way air turbine which is

Extended author information available on the last page of the article

Published online: 24 March 2025

generally substantially more efficient than a Wells or self-rectifying turbine. However, to fully exploit this improved efficiency, the losses from the release valve system must be very small so that the total wave-to-wire efficiency gain is enough to offset the extra costs associated with the added complexity of the device.

The experimental measurements used in this study were conducted at the Technical University of Denmark (DTU) and are reported in Joensen et al. (2023) and Trevino (2020). The study was blind, in the sense that the participants did not have access to the measurements until after their numerical calculations were submitted. The models applied by the participants include several variations of weakly nonlinear potential flow theory and several different commercial CFD (Navier–Stokes solver) codes. The goal of the study is to identify and highlight the modeling challenges associated with analyzing WECs in general, and OWC-type WECs in particular. As can be seen in the results shown here, even for a relatively simple case of one fixed OWC chamber, a substantial spread in the numerical calculations is found. For the weakly nonlinear potential flow models, different strategies for including the orifice plate pressure and the one-way release valve lead to quite different results. For the CFD calculations, again different strategies are adopted to model the air flow and valve system, and different choices are made for turbulence models, grid resolution, and other numerical parameters, all of which leads to significant scatter in the calculated results. Both compressible and incompressible CFD codes were used, but no significant influence from air compressibility was identified due to the small scale of the experiments. It is not the intention to provide a comprehensive review of OWC modeling approaches to date; rather, a comparison of modeling approaches for a novel OWC system is provided. However, the interested reader is referred to Zhao and Ning (2024), Rosati et al. (2022), Falcão and Henriques (2016), Zabala et al. (2019), Opoku et al. (2023) and the references contained therein.

2 Experimental measurements

The experimental measurements are briefly described here, while more complete details can be found in Joensen et al. (2023) and Trevino (2020). The dimensions and layout of Flume 1 of the DTU hydraulics laboratory are shown in Fig. 1, and the chamber model is shown in Fig. 2.

As shown in Fig. 1, the flume is 25 m long, 0.6 m wide and the water depth was set to $h = 0.65$ m. The single chamber model is attached to one wall of the flume so that this acts as a plane of symmetry and the water column is activated sideways by the passing waves. The model is at 1:50 scale with respect to a full-scale model. The geometry of the full-scale chamber is based on one of the 20 double-chambers on the KNSwing device designed for the Danish North Sea where the average wave period is around 6 s. This is intended to provide a relatively simple fixed test case suitable for an initial benchmark study. The dimensions of the chamber are shown in Table 1. The origin of the coordinate system is at the center of the chamber along the tank wall with the z-axis pointing up from the still water level.

The full-scale natural resonance period of the chamber is close to the expected mean peak wave period of 6 s. A lid is placed on the top of the chamber and fitted with a pressure sensor to measure the internal chamber air pressure relative to atmospheric pressure. Two resistive wave probes pass through the lid to measure the internal free surface at two locations along the cross-tank centerline of the chamber. To model an impulse turbine, there is an orifice in the middle of the lid of diameter 0.016 m at model scale. This diameter was chosen based on a simple optimization procedure described in Joensen et al. (2023), §4.2, where it was found to give the largest integrated CWR over all wave frequencies. For conventional two-way power absorption, the three circular flanges at the top of the chamber are closed with air tight caps. For one-way absorption, air hoses connect these openings to a box at the side of the tank which is fitted with a lightweight balsa wood flap of the same area as the chamber internal surface. Two versions of the flap were built to allow for venting on either the up- or the down-stroke as shown in Fig. 2.

A series of monochromatic incident wave conditions were run, as shown in Table 2. Here, T is the wave period, λ the length and $H = 2A$ the height with A the wave amplitude. H_1 and H_2 correspond to wave steepness values of $\epsilon = H/\lambda = [0.025, 0.04]$, respectively, corresponding to nearly linear conditions. Data was acquired at 512 Hz and up to $t = t_{\max}$, which represents the time for the wave front to travel from the wavemaker to the beach and back to the chamber according to the linear group velocity. By restricting the record to this length, we avoid any possible reflections from the beach.

Each wave condition shown in Table 2 was run first without the chamber in the tank in order to establish the undisturbed incident wave conditions. The chamber was then placed in the tank and each wave condition was run with the chamber open (no power take off (PTO) damping), with two-way energy absorption, with up-stroke venting and with down-stroke venting. Three repetitions were run for all cases in order to estimate the uncertainties.

3 Theory

This section briefly reviews the theory behind the two numerical methods that were applied in this benchmark study, i.e., weakly nonlinear potential flow theory and the Reynolds-

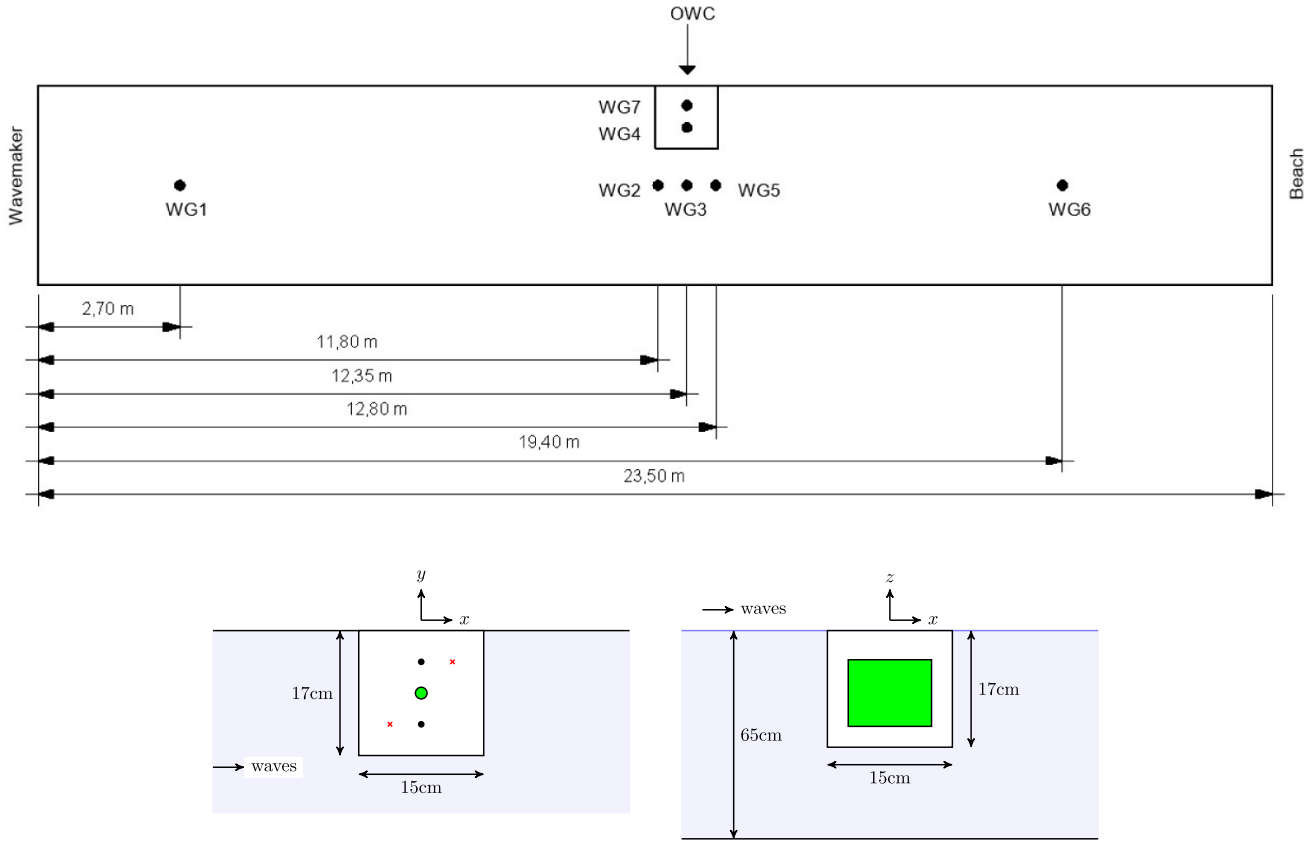

Fig. 1 Layout of the experiments and the chamber. In the bottom left figure, the green circle represents the orifice, the blue circles indicate WG7 and WG4, and the red crosses mark the locations of the pressure sensors in the chamber lid

Table 1 Full-scale and model-scale dimensions of the OWC

Parameter	Model scale	Full scale	Description
L [m]	0.15	7.5	Total chamber length
L_i [m]	0.12	6	Internal chamber length
B [m]	0.10	5	Internal chamber width
D [m]	0.15	7.5	Internal water column depth
T_0 [s]	0.818	5.78	Resonance period
d_o [m]	0.016	0.8	Orifice diameter

averaged Navier–Stokes equations (CFD). For more in-depth reviews of the history and analysis of WECs in general and OWCs in particular, see for example Falnes (2002), Cruz (2008), Drew et al. (2009), Falcão (2010), McCormick (2007) and Heath (2012).

3.1 The Navier–Stokes equations (CFD)

The flow of a Newtonian fluid is governed by the Navier–Stokes equations (see for example Batchelor 1967) expressing conservation of mass and momentum as

$$\frac{\partial \rho}{\partial t} + \frac{\partial}{\partial x_j}(\rho\, u_j) = 0 \tag{1a}$$

$$\frac{\partial (\rho\, u_i)}{\partial t} + \frac{\partial}{\partial x_j}(\rho u_i\, u_j) = \frac{\partial T_{ij}}{\partial x_j} + f_i, \tag{1b}$$

where ρ is the fluid density, $u_j = [u_1, u_2, u_3]$ is the velocity vector in a Cartesian coordinate system with the x_3-axis pointing vertically upwards and $f_i = [0, 0, -\rho g]$ the gravitational source term. Here, the summation convention is adopted where repeated indices implies a sum from one to three. For a Newtonian fluid, the stress tensor is given by

$$T_{ij} = -\left(p + \frac{2}{3}\mu \frac{\partial u_k}{\partial x_k}\right)\delta_{ij} + \mu\left(\frac{\partial u_i}{\partial x_j} + \frac{\partial u_j}{\partial x_i}\right), \tag{2}$$

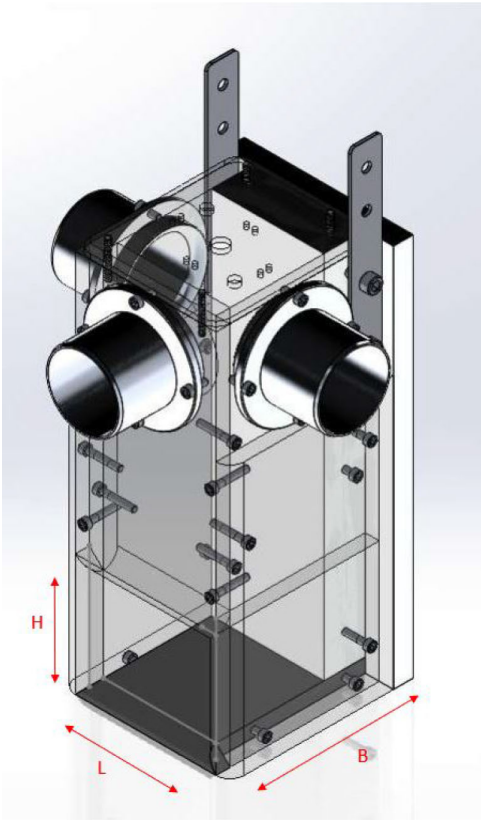

(a) 3D CAD model of the OWC chamber.

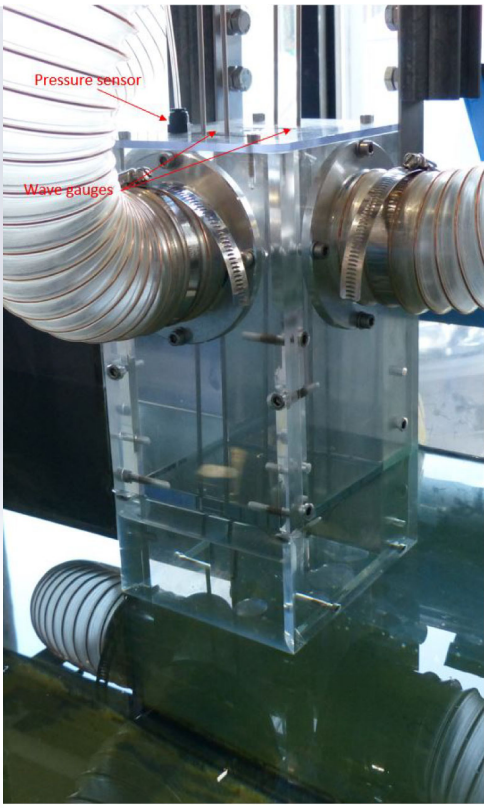

(b) Photograph of the OWC chamber in place for tests.

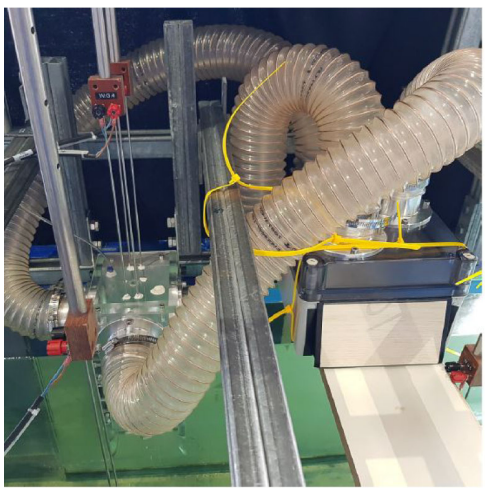

(c) Photograph of the OWC chamber, hoses and valve box.

Fig. 2 OWC chamber used in the experiments. . (From Joensen et al. (2023))

with p the fluid pressure, μ the dynamic viscosity, and δ_{ij} the Kronecker delta function. If the fluid is assumed to be incompressible, then Eq. (1) reduces to

$$\frac{\partial u_i}{\partial x_i} = 0 \tag{3a}$$

$$\frac{\partial u_i}{\partial t} = -\frac{\partial (u_i\, u_j)}{\partial x_j} + \nu \frac{\partial^2 u_i}{\partial x_j^2} - \frac{1}{\rho}\left(\frac{\partial p}{\partial x_i} - f_i\right), \tag{3b}$$

with $\nu = \mu/\rho$ the kinematic viscosity.

3.2 Weakly nonlinear potential flow theory

If the fluid viscosity is neglected and the flow is assumed to be irrotational, then the incompressible Navier–Stokes equations reduce to a potential flow. The fundamentals of linear potential flow theory are covered in detail by, for example,

Table 2 Monochromatic wave conditions tested in the experiments

T (s)	λ (m)	H_1 (m)	H_2 (m)	t_{max} (s)
0.57	0.51	0.013	0.021	84
0.74	0.85	0.021	0.034	65
0.78	0.94	0.024	0.038	62
0.79	0.98	0.025	0.039	60
0.81	1.02	0.026	0.041	59
0.82	1.05	0.026	0.042	58
0.83	1.07	0.027	0.043	58
0.84	1.11	0.028	0.044	57
0.86	1.15	0.029	0.046	55
0.90	1.26	0.032	0.050	52
0.98	1.49	0.037	0.060	47
1.15	1.98	0.050	0.079	38
1.31	2.48	0.062	0.099	32
1.47	2.98	0.074	0.119	27
1.64	3.46	0.087	0.138	24

the classic textbooks of Newman (2017) and Falnes (2002). The specific application of the theory to OWC-type WECs described here closely follows the presentations found in Bingham et al. (2021) and Joensen et al. (2023).

We adopt the *generalized modes* approach of Newman (1994) to describe the motions of the chamber internal free surface. The interaction of a floating body with ocean waves is described by the generalized response vector $x_j(t)$, $j = 1, 2, \ldots, 6 + M_g$, where $j = 1, 2, \ldots, 6$ represent the rigid-body modes and $j = 7, 8, \ldots, M_g$ are the generalized modes. We assume that the incident waves can be described by a superposition of linear long-crested monochromatic components, each of which has a radian frequency ω, an amplitude A and a direction of propagation β measured from the positive x-axis,

$$\eta_0(x, y, t) = \Re\{A e^{i[\omega t - k(x\cos\beta + y\sin\beta)]}\}, \tag{4}$$

where $\Re$ indicates the real part and $i = \sqrt{-1}$ is the imaginary unit. The wavenumber k is given by the linear dispersion relation

$$\omega = \sqrt{gk\tanh kh},\ c = \frac{\omega}{k},\ c_g = \frac{c}{2}\left(1 + \frac{2kh}{\sinh 2kh}\right), \tag{5}$$

and c and c_g are the phase and group velocities, respectively. The wavelength $\lambda = 2\pi/k$ and the wave period is $T = 2\pi/\omega$. The steady-state response to this wave component is $x_j(t) = \Re\{\xi_j(\omega, \beta)\, e^{i\omega t}\}$, where ξ_j is the complex motion response phasor which is found by solving the equations of motion in the frequency domain,

$$\sum_{k=1}^{6+M_g}\Big[-\omega^2\Big(M_{jk} + A_{jk}\Big) + i\omega\Big(B_{jk} + B^0_{jk}\Big) + C_{jk}\Big]\xi_k = X_j,$$
$$j = 1, 2, ..., 6 + M_g. \tag{6}$$

Here, M_{jk} is the body inertia matrix, A_{jk} and B_{jk} are the hydrodynamic added mass and damping coefficient matrices, C_{jk} is the hydrostatic restoring force coefficient matrix, and X_j is the wave excitation force vector. B^0_{jk} is an external damping coefficient matrix that is used to model the effects of the air turbine PTO on the OWC chamber motion.

Each of the generalized body modes is defined by the boundary conditions

$$\left.\begin{aligned}\frac{\partial\phi_j}{\partial z} &= w_j(x, y), \text{ on } S_i\\ \frac{\partial\phi_j}{\partial n} &= 0, \qquad\quad \text{on } S_b\end{aligned}\right\}\ j = 7, 8, ..., 6 + M_g, \tag{7}$$

where S_i is the internal free surface of the OWC chamber, S_b is the wetted body surface, and $w_j(x, y)$ is the vertical displacement shape function of generalized mode j. Here, the coordinate system has its origin at the center of the double-chamber with the x-axis directed along the tank length and the z-axis pointing vertically upwards from the still water surface. From previous studies using this chamber (e.g. Bingham et al. 2015), the only significant chamber response modes for the two-way absorption strategy are the *piston mode* and the first transverse sloshing mode which are defined by the shape functions

$$w_7 = 1,$$
$$w_8 = \cos[k_l(y - y_0)]. \tag{8}$$

Here, $k_l = \pi/B$ with $B = 5$ m the internal chamber width, and $y_0 = 1.5$ m the distance from the chamber centerline to the inside wall of the chamber (both dimensions at full scale). For the one-way absorption strategy the internal motion of the chamber surface is more complicated and can include longitudinal modes, but these motions cannot be identified in measurements from only two locations along the transverse chamber centerline, so they were not included in the reference potential flow calculations. The CFD calculations, however, are able to capture them, as discussed further below. As shown in Sect. 3.2.1, the equivalent linearized PTO damping coefficient B^0_{77} is proportional the piston-mode response amplitude $|\xi_7|$, which makes the equations dependent on the incident wave amplitude and thus weakly nonlinear.

As originally noted by Cummins (1962), the equivalent problem written directly in the time domain takes the form

$$\sum_{k=1}^{6+M_g} \left[(M_{jk} + A^{\infty}_{jk})\ddot{x}_k(t) + \int_{-\infty}^{t} K_{jk}(t-\tau)\dot{x}_k(\tau)\mathrm{d}\tau + C_{jk}x_k(t) \right] = F_{jD} + F_{j0}, \quad j = 1, 2, ..., 6 + M_g, \tag{9}$$

where $A^{\infty}_{jk} = A_{jk}(\infty)$ is the infinite frequency limit of the added mass coefficient and the over-dots represent time derivatives. The radiation impulse response functions, K_{jk}, and the diffraction force, F_{jD}, are related to the frequency-response functions through the Fourier transforms

$$K_{jk}(t) = \frac{2}{\pi}\int_0^{\infty} B_{jk}\cos\omega t\,\mathrm{d}\omega,$$

$$K_{jD}(t) = \frac{1}{2\pi}\int_{-\infty}^{\infty} X_j \mathrm{e}^{\mathrm{i}\omega t}\,\mathrm{d}\omega, \tag{10a}$$

$$F_{jD}(t) = \int_{-\infty}^{\infty} K_{jD}(t-\tau)\,\eta(\tau)\,\mathrm{d}\tau = \int_{-\infty}^{\infty} \frac{X_{jD}}{A}\hat{\eta}\,\mathrm{e}^{-\mathrm{i}\omega t}\,\mathrm{d}\omega, \tag{10b}$$

$$\hat{\eta}(\omega) = \int_{-\infty}^{\infty} \eta(t)\,\mathrm{e}^{\mathrm{i}\omega t}\,\mathrm{d}t, \tag{10c}$$

where η is a particular incident wave elevation measured at the origin of the coordinate system. Here, K_{jD} is the diffraction impulse response function, and the two equivalent forms of F_{jD} indicate how the wave excitation force can be computed in either the time- or frequency domains when the incident wave elevation signal is known for all time. Other external forces applied to the body, e.g. by the air turbine or a mooring system, are represented by $F_{j0}(t)$ and can be nonlinear.

3.2.1 Incompressible flow model of the PTO damping

Although air compressibility effects are important at full scale, the above described model-scale experiments are at such a small scale that these effects are assumed to be negligible. Assuming an incompressible flow, there is a quadratic relationship between the air volume flux through the orifice plate, Q, and the pressure inside the chamber, p given by

$$p(t) = \frac{1}{2}\rho_a\left(\frac{1}{C_d S_o}\right)^2 Q(t)^2 \mathrm{sign}(Q), \tag{11}$$

where ρ_a is the air density, S_o is the area of the orifice, and C_d is a head-loss coefficient which must be determined experimentally. Only the piston mode, $j = 7$, contributes to the flux so

$$Q(t) = S_c\dot{x}_7, \tag{12}$$

where S_c is the internal free surface area. The applied force from the orifice plate is then given by

$$F_{70} = -S_c R_0 \dot{x}_7^2\,\mathrm{sign}(\dot{x}_7), \quad R_0 = \frac{1}{2}\rho_a\left(\frac{S_c}{C_d S_o}\right)^2. \tag{13}$$

This force can be directly applied in the time domain, but in the frequency domain, it needs to be expressed by an equivalent linearized damping coefficient. As shown by e.g. Bingham et al. (2021), by assuming a sinusoidal flux and equating the linear and nonlinear power loss per cycle, the equivalent linear damping coefficient is given by

$$B^0_{77} = \frac{8}{3\pi}\omega S_c R_0 |\xi_7|. \tag{14}$$

Because this coefficient is a function of the magnitude of the response, the equations of motion must be solved iteratively at each frequency and wave steepness $\epsilon = H/\lambda$.

For one-way absorption, we assume a perfect venting valve system such that $F_{70} = 0$ when $\dot{x}_7$ is greater than zero for up-stroke venting or less than zero for down-stroke venting, and Eq. (13) is applied on the other half-cycle of the chamber motion. In the frequency domain, since power is only extracted on one half of the cycle, Eq. (14) is simply divided by two.

The choice of C_d

From earlier work with this chamber Bingham et al. (2015), quasi-static measurements for an orifice plate of diameter 14 mm suggested a value of $C_d = 0.64$. However, for the current set of experimental measurements with two-way absorption and an orifice plate of 16 mm diameter, a best fit based on Eq. (11) and the measured dynamic pressures and fluxes gave the value $C_d = 0.7$. This value was, therefore, chosen for post-processing of the experimental data and by the teams using this model for the orifice plate damping. There is however, significant uncertainty in this value, and further investigation of this is suggested.

3.3 Absorbed power

The absorbed hydrodynamic power $P(t) = p(t)\,Q(t)$, and the average over a wave period is given by

$$\bar{P} = \frac{1}{T}\int_0^T P(t)\,\mathrm{d}t. \tag{15}$$

The capture width ratio (CWR) is the average absorbed power normalized by the available wave energy flux and is given by

$$\bar{W} = \frac{\bar{P}}{\frac{1}{2}\rho g A^2 c_g L}, \tag{16}$$

where the length along a wave crest, L, is taken to be the chamber length along the x-axis. As discussed in more detail in Joensen et al. (2023), it was determined to be generally more reliable in the experimental measurements to compute Q from p using Eq. (11), with $C_d = 0.7$ because evaluating the flux from only two wave gauge signals can be quite error-prone. This does, however, introduce significant uncertainty into the experimental results.

4 The benchmark study

The participants in the benchmark study were provided with all of the experimental conditions including the geometry of the flume and the chamber, and the measured incident wave records for each test condition at the location of the chamber transverse centerline from WG 3. Experimental measurements of the piston-mode response for the open chamber with no orifice plate attached were also provided. The linearized potential flow coefficients for the chamber were provided to participants who wanted to use them.

4.1 Reference potential flow hydrodynamic coefficients

Reference coefficients for the chamber were computed using the commercial radiation/diffraction software WAMIT Newman and Lee (2023), following the special procedure for OWCs proposed by Prof. Newman and described in Bingham et al. (2021). Figure 3a shows the high-order panel discretization of the submerged chamber surface that was used for computing the coefficients at finite frequency $0 < \omega < \omega_{max}$. The bright green patches here are the internal chamber surfaces S_i upon which generalized modes are applied.

In order to approximately model the relatively narrow width of the wave flume, the calculations are performed using two reflections of the model about the position of the side wall, as shown in Fig. 3c. Here, the y-distance between the centerline of each model is twice the tank width of 0.6 m, or 30 m in full scale.

As noted above, we only consider two generalized modes of the internal free surface: $j = 7$, the piston mode, and $j = 8$, the first transverse sloshing mode. These motions are visualized in Fig. 4 which shows how the two-mode approximation of the internal surface motion relates to the geometry of the chamber. The dashed green lines indicate the two internal wave probes which are offset by a distance of $c_1 = c_2 = 10$ mm (at model scale) from the chamber walls. The dotted blue line indicates the piston mode and the solid blue line the sum of a piston and the first standing-wave mode.

The resulting added mass and damping coefficients are shown in Fig. 5, where we note that the $\omega = \infty$ limit is plotted at $\bar{\omega} = \omega\sqrt{L/g} = 6$, with $g = 9.81\,\mathrm{m/s^2}$ the gravitational acceleration and $L = 0.15$ m the total chamber length (at model scale). Here, we can see that the damping coefficient is rapidly convergent for all frequencies, while the high-frequency range of the added mass converges much more slowly. This is due to the fact that the mixed source/dipole boundary element method (BEM) used by WAMIT is singular at $\omega = \infty$ when the body has panels lying directly on the free surface. This singularity also leads to ill-conditioned systems at high, but finite, frequency. In order to use the WAMIT calculations in the time domain, it is critical to have an accurate value for the $\omega = \infty$ limit, especially in this case where the *mass* corresponding to the chamber motion is exactly zero. To compute this value correctly, we adopt the procedure suggested by Prof. Newman, and described in Bingham et al. (2021). First, a new geometry is created by reflecting the original geometry about the $z = 0$ plane, as shown in Fig. 3b. The water depth is then set to $2h$ and the chamber is submerged to a depth h. Finally, the internal chamber surface (the green patch in Fig. 3b) is defined to be a *dipole surface*. Now the problem can be solved accurately at $\omega = \infty$ and the results represent twice the value for the real geometry (since there are now effectively two bodies in the domain). The values plotted at $\omega\sqrt{L/g} = 6$ in Fig. 5 were computed using this recipe. Finally, we note that the first standing-wave mode, ξ_8, is nearly *waveless*, i.e., the added mass is essentially constant and the damping is nearly zero relative to the piston-mode values.

Convergence of the wave exciting force coefficients for the two considered modes is shown in Fig. 6, where we can see that these coefficients are also rapidly convergent. Figure 7 compares the WAMIT free-response RAO with the response computed in the time domain using the open-source package DTUMotionSimulator Bingham and Read (2023) to confirm that the above-described strategy for computing the infinite frequency limits of A_{jk} works correctly. This package solves Eq. (9) via the Fourier transforms of Eq. (10) and a direct evaluation of the convolution integral.

All of the hydrodynamic coefficients, described above along with the associated hydrostatic and inertia matrices, were provided to all participants as reference values. Based on previous work with this chamber, the value of $C_d = 0.7$ was adopted for this study.

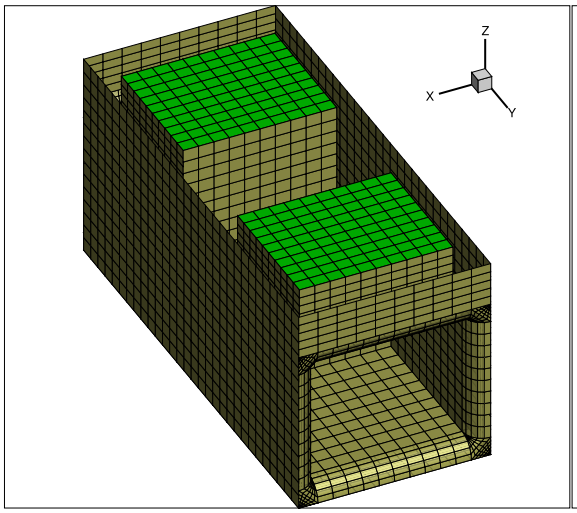

(a) The submerged chamber geometry, finite ω.

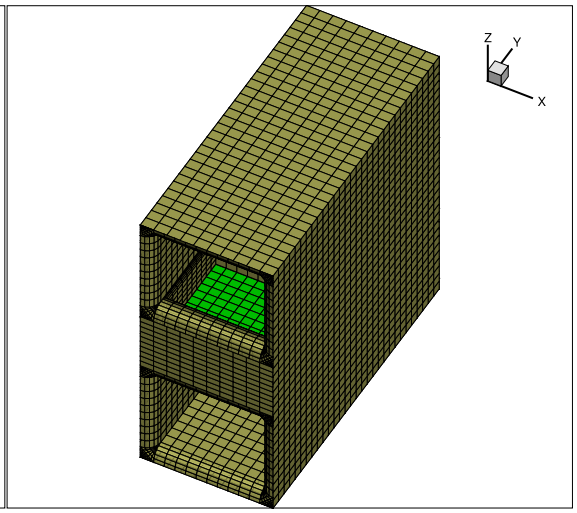

(b) The chamber geometry for $\omega = 0, \infty$.

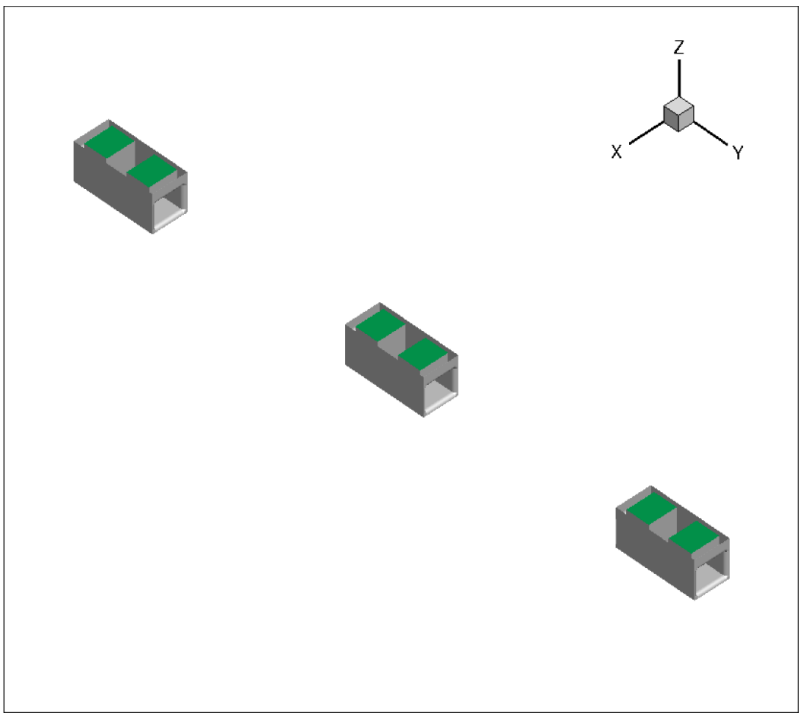

(c) Two image geometries are used to approximate the effects of the second flume wall.

Fig. 3 High-order panel geometries for WAMIT calculations. The bright green patches are the internal chamber surfaces where the generalized modes are applied. Two images are used to approximate the second wall of the flume

4.2 The models adopted by the participating teams

This section describes the different numerical models that were adopted by each of the participating teams. They are presented, roughly speaking, in increasing order of fidelity.

4.2.1 Ramboll Mathcad calculations

The results provided by Ramboll are calculated using Mathcad Prime and the reference WAMIT data discussed above. The theory used is the linear theory in the frequency domain with only one degree of freedom, $j = 7$ the piston mode. The results provided by the Ramboll Mathcad script are useful to compare with the other potential flow calculations

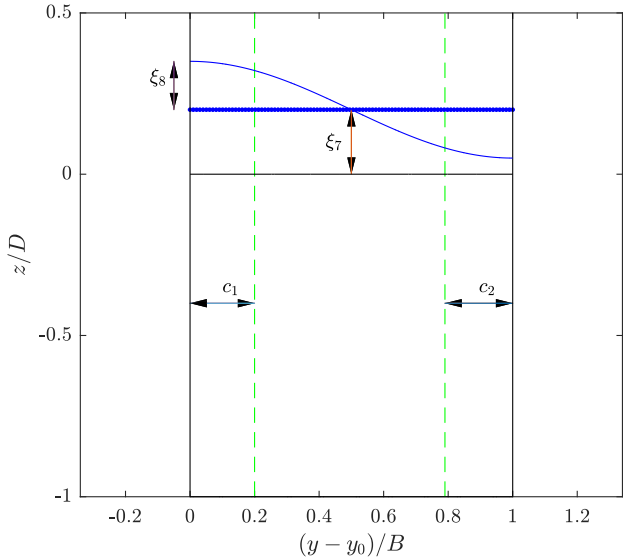

Fig. 4 The two-mode decomposition of the chamber surface motion

which include more modes and/or more nonlinearity. The reference WAMIT coefficients are imported into a Mathcad Prime worksheet. The discrete hydrodynamic parameters are then fitted using spline functions to provide smooth function of wave period for further calculations. In the Mathcad worksheet, the hydrodynamic formulas have been integrated. This means that RAO's of the OWC surface heave, the pressure as well as the CWR can be calculated for the given test case and validated against the experimental results and similar calculations. The Mathcad worksheet is intuitive and easy to read, and it offers the possibility to study the effect of changing, i.e., the size of the orifice, scale of the chamber etc.

4.2.2 The Maynooth University (MU)/Dundalk IT potential flow model

A one-degree-of-freedom (1-DOF), time-domain numerical model, in which air is assumed incompressible, of the DTU OWC is developed. The chamber is assumed to operate in three-dimensional space, and no account of reflections from the side wall of the tank is considered. The MU/DkIT model is based on the well-known Cummins Equation (9) and uses BEM software codes, such as WAMIT, to determine the necessary hydrodynamic and hydrostatic parameters. The geometry used to calculate hydrodynamics from WAMIT is shown in Fig. 8. The rationale for the difference in this setup when compared to the one in Sect. 4.1 is to allow for the assessment of the importance of the reflections in the setup. The resultant hydrodynamic parameters are used to develop a time domain 1-DOF (pumping) model, in state-space form, for a two-way absorption case. For further details of the model and the associated assumptions, readers are referred to Bingham et al. (2021).

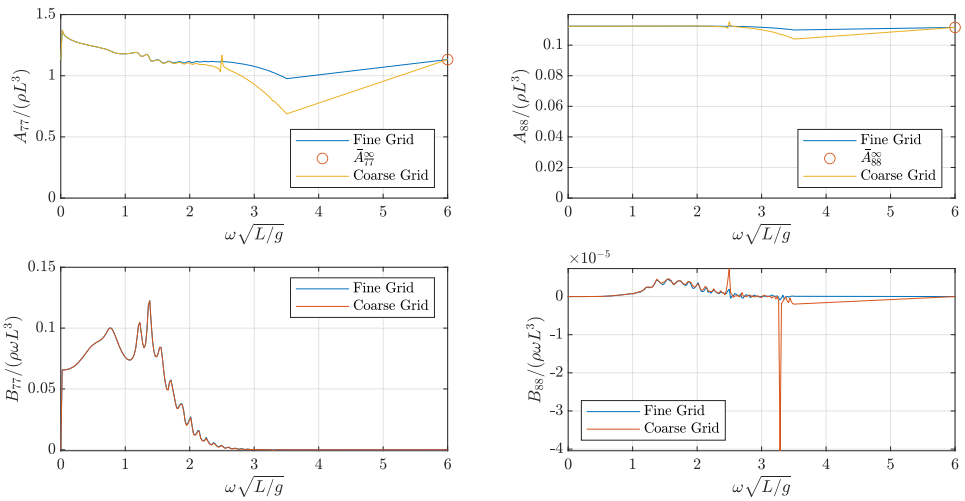

Fig. 5 Added mass and damping coefficients for the chamber piston (left) and first standing-wave (right) response. The $\omega = \infty$ limit is plotted at $\bar{\omega} = 6$

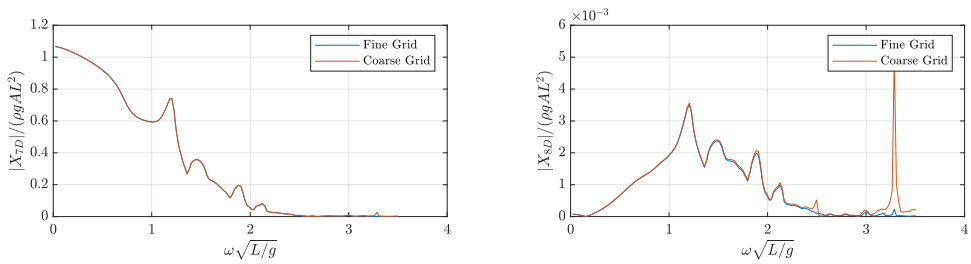

Fig. 6 The magnitude of diffraction excitation forces

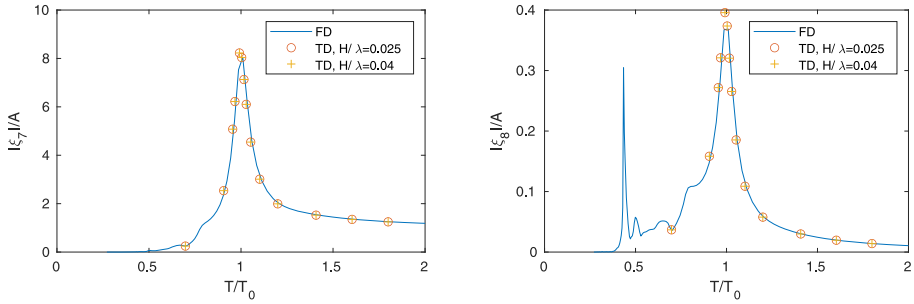

Fig. 7 Validation of the computed time-domain free-response RAOs of the chamber with the original WAMIT results. $T_0 = 0.82$ s is the natural period of the piston mode response

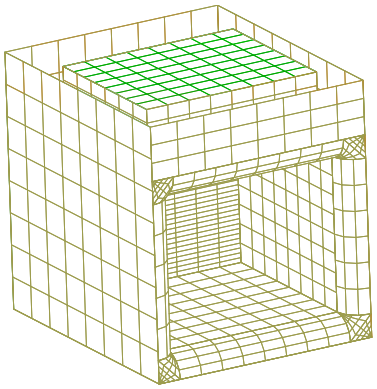

Fig. 8 The single chamber OWC setup used in the MU/DkIT model

For the one-way absorption cases (up-stroke/down-stroke venting), a *bang-bang* strategy is employed to model the effect of the one-way valve. The chamber gauge pressure is manually set to zero depending on the direction of the water column (up-stroke/down-stroke venting). The 1-DOF model is simulated in MATLAB as sets of ODEs in matrix form (state space), which are solved using the ODE solvers available in MATLAB. The parametric approximations are used for both the radiation and excitation forces using the methods described in Pena-Sanchez et al. (2019) and Guo et al. (2018).

4.2.3 The MARIN potential flow model

The calculations were performed using MARIN's wave diffraction solver DIFFRAC (MARIN 2022). This program solves the linearized velocity potential in the frequency domain, assuming an inviscid, homogeneous and incompressible fluid. Boundary conditions apply at the bottom, the water surface, and at the user-defined body (in this case the OWC chamber); the latter is represented through a panel mesh.

The damping by the orifice leads to an excess pressure inside the chamber, which is accounted for through a modified relation for the boundary condition at the water surface inside the chamber (see, e.g., Liu et al. 2010):

$$\frac{\partial \phi(t)}{\partial t} + g\eta(t) + \frac{p(t)}{\rho} = 0 \tag{17}$$

Here, ϕ is the velocity potential; η is the water surface elevation; p is the excess chamber pressure; and ρ is the water density. The excess chamber pressure scales non linearly to the air flow rate Q through Eq. (11). This nonlinearity needs to be overcome to solve the system of equations in the frequency domain. In line with the descriptions in Sect. 3.2.1, a linearized damping coefficient is introduced, replacing Eq. (11) through

$$p(t) = \frac{B_{77}^0}{S_c^2} Q(t), \tag{18}$$

where B_{77}^0 is the equivalent linearized damping coefficient as per Eq. (14) that leads to the same power loss over one wave cycle as the nonlinear relation.

By neglecting air compressibility, Q can be equated to the vertical fluid velocity integrated over the chamber free surface area S_c:

$$Q(t) = \iint_{S_c} \frac{\partial \eta(t)}{\partial t} \mathrm{d}S_c \tag{19}$$

With $\frac{\partial \eta}{\partial t} = \frac{\partial \phi}{\partial z}$ at the water surface, Eqs. (17)–(19) can be combined into

$$\frac{\partial^2 \phi}{\partial t^2} + g\frac{\partial \phi}{\partial z} + \frac{B_{77}^0}{\rho S_c^2} \iint_{S_c} \frac{\partial^2 \phi}{\partial t \partial z} \mathrm{d}S_c = 0 \tag{20}$$

which in a frequency domain formulation reads

$$-\omega^2 + g\frac{\partial \phi}{\partial z} - \frac{B_{77}^0}{\rho S_c^2} \iint_{S_c} i\omega \frac{\partial \phi}{\partial z} \mathrm{d}S_c = 0. \tag{21}$$

As noted in Sect. 3.2.1, B_{77}^0 depends on the chamber response (see Eq. (14)), which in turn depends on the orifice damping. Similar to Bingham et al. (2015), this is resolved through diffraction calculations in which B_{77}^0 is iteratively updated based on the computed chamber response, until

results converge. For the cases with one-way damping, following Joensen et al. (2021), the linearized orifice damping is halved. Viscous losses (e.g., due to friction or sloshing inside the chamber) are not resolved by the potential flow solver, but are instead accounted for by the lid approach described in Pauw et al. (2007) and are in the present study tuned for each wave steepness based on the open water response.

The iterative calculations were performed for each tested combination of theoretical wave period and amplitude, resulting in complex RAOs of the flow rate Q inside the chamber. In post-processing, the measured undisturbed water surface time trace of each test was transferred to the frequency domain and combined with the RAO to obtain the response spectrum of Q inside the chamber. The response spectrum was then transformed back to the time domain to allow comparison of $Q(t)$ at time-series level. The nonlinear pressure relation in Eq. (11) was used to compute time series of pressure and absorbed power based on $Q(t)$. For the cases with one-way damping, time series of flow rates and pressures were clipped to 0 when venting occurs based on the sign of $Q(t)$.

We note that all calculations were performed for a single chamber in open water, so no channel walls were included.

4.2.4 The NREL potential flow model

WEC-Sim (Yu et al. 2014; WEC-Sim Development Team 2023) was used in the NREL simulations, following the weakly nonlinear potential flow theory described in Sect. 3.2. The WAMIT-generated reference potential flow hydrodynamic coefficients presented in Sect. 4.1 were used in the in WEC-Sim simulations, and the nonlinear PTO force was calculated using Eq. (13) with a C_d value of 0.7 and directly implemented as a quadratic damping term in the time domain for two-way energy extraction (Bingham et al. 2021).

For one-way absorption cases (i.e., up-stroke venting and down-stroke venting), the WEC-Sim model was modified to include an additional MATLAB function block when calculating the PTO force, where Eq. (13) was applied for only a half-cycle of the chamber motion and $F_{70} = 0$ was enforced for the other half of the chamber motion.

To capture the internal chamber surface motion, the generalized mode approach was also used in WEC-Sim. The additional modes were implemented in a state-space form when solving the equations of motion, and these state-space-form equations were coupled to the default system dynamics solver provided by the MATLAB Simscape Multibody Toolbox to solve the entire system of equations (Eq. (9)). More details on the development of the generalized mode approach method in WEC-Sim and examples of implementing generalized mode analysis to solve WEC-liked systems were presented in (Guo et al. 2017; Bingham et al. 2021).

4.2.5 The Saga University CFD model

To solve the two-way case, olaFlow (Higuera 2017) was applied. olaFlow is an open-source project that extends wave capabilities to OpenFOAM (OpenCFD 2023). The active wave generation and absorption functions of OpenFOAM have been improved (Higuera et al. 2015). In addition, although it is not used in this paper, a calculation function for porous objects has been added. olaFlow, like OpenFOAM, uses the finite-volume method to solve the continuity equations and the Reynolds-averaged Navier–Stokes equations (RANS). In this paper, the flows were calculated using a combination of OpenFOAM v1912 and olaFlow v2012.

The computational domain was $x \in [-4, 4]$, $y \in [-0.6, 0]$, $z \in [-0.65, 0.35]$. The still water level was set to $z = 0$. An unstructured grid was employed for the calculations. The grid size near the orifice was 2 mm. The grid size around the OWC was 10 mm and increases outward from the OWC to 50 mm at the inlet and outlet boundaries. The total number of cells was approximately 350,000. The mesh used for the calculations is shown in Fig 9.

The wave velocity was set at the inlet, and the wave velocity was absorbed at the outlet. Slip conditions were applied at the tank walls. At the upper boundary, the atmospheric pressure was set, and at other boundaries the normal derivative of the pressure was set to zero. As a first step, we assumed laminar flow and did not use a turbulence model. The time step is variable, and was selected so that the Courant number did not exceed 0.8. The average time step size was 5.7E−4 s, which corresponds to 7/10,000 of the incident wave period.

4.2.6 The RISE CFD model

The two-way absorption simulations were performed using the two-phase incompressible RANS solver interFoam available in the open-source framework OpenFOAM-v2212 (OpenCFD 2023). The OpenFOAM framework is based on a cell-centered 2nd-order finite-volume method on unstructured polyhedral cells (Weller et al. 1998). In interFoam, the air–water interface is handled by an algebraic volume of fluid method in combination with an artificial interface compression scheme. The standard k-ω-SST turbulence model of Menter et al. (2003) is used, together with a continuous wall function approach.

Compared to the experimental setup, the computational domain is truncated in length while keeping the spanwise dimension equal to the test setup: $x \in [-3, 3]$, $y \in [-0.6, 0]$, $z \in [-0.65, 0.65]$ m with the OWC placed at $x = 0$, see Fig. 10. This corresponds roughly to 3 wavelengths upstream and downstream of the OWC. The computational mesh is created using the snappyHexMesh utility in OpenFOAM, which generates oct-tree hexahedral-dominated meshes from STL surfaces of the body. The mesh

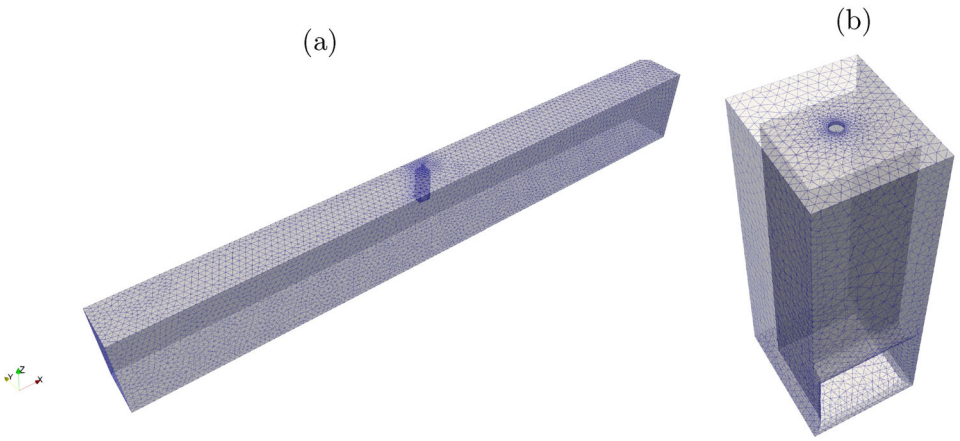

Fig. 9 SAGA grid for two-way absorption. **a** The entire fluid domain and **b** the OWC

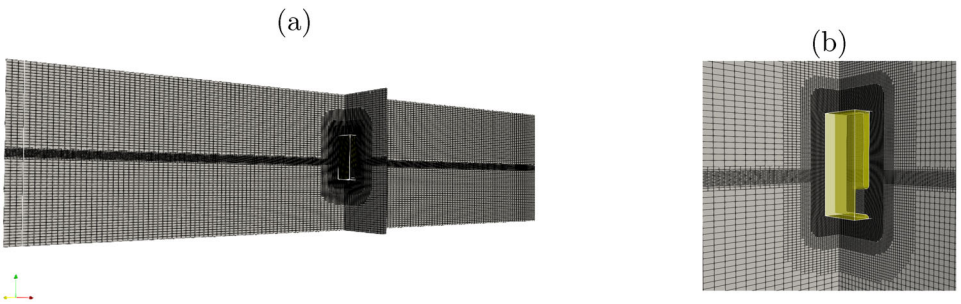

Fig. 10 The CFD mesh used in the RISE simulations. **a** Entire computational domain and **b** zoom in on the OWC

is rather coarse—only 2.7M cells—with 50 cells per wavelength and 10 cells per wave height. There are refinement boxes around the free surface and the OWC. The boundary layers are resolved by 5 cells with a maximum y^+ typically below 100.

The OWC boundaries are set as no-slip wall boundaries, whereas the tank side boundaries are treated as walls with a slip condition applied. The bottom boundary is also treated as a slip wall. The upper atmospheric boundary is set to a zero total pressure condition. The numerical schemes used in the simulations are the second-order van Leer scheme for convection terms, second-order central differences for diffusion terms, whereas the turbulence equations are solved using the first-order upwind method. The time-stepping is carried out using the first-order backward Euler scheme with a CFL number of 0.9.

Initially wave generation was carried out with the native wave generation functions in OpenFOAM, due to Higuera et al. (2013). However, as the wave tank was rather short, waves reflected off the OWC reached the wave generation boundary and caused severe problems. Thus, wave generation/absorption in the RISE simulations has been performed using 1.5 m wide relaxation zones (Jacobsen et al. 2012).

Figure 11 shows snapshots of the jet through the orifice during exhale and inhale of the two-way absorption case. There is no noticeable sloshing inside the OWC. A formal solution verification using the least-squares approach of Eça and Hoekstra (2014) with three meshes between 16.2M and 2.7M cells showed that the CFD solutions are a bit uncertain in terms of absorbed power. Convergence was oscillatory and the estimated uncertainties were >7% and >12% for the H_1 and H_2 cases, respectively.

4.2.7 The NREL-CFD model

The high-fidelity CFD code, STAR-CCM+ was used to study the wave energy extraction PTO system with different energy absorption modes including two-way, one-way up-stroke, and one-way down-stroke absorption cases. An implicit, three-dimensional, compressible, unsteady RANS model was applied herein. The shear stress transport (SST) $k-\omega$ model was chosen to model the turbulence in the CFD domain. The volume-of-fluid method based on the High-Resolution Interface-Capturing scheme was also used to model the interface between air and water at the free surface. Second-order schemes were chosen for both the spatial and temporal discretization. A time step size of $T/\Delta t = 400$ was chosen where T is the wave period. The semi-implicit method for pressure-linked equations approach was chosen to solve the pressure–velocity coupling with 15 iterations per time step. The under-relaxation factors for velocity and pressure were 0.8 and 0.4, respectively.

In the current study, the computational domain's upstream and downstream dimensions were bounded at 4 times the wavelength (4λ) from the oscillating water column center. Only half of the OWC device was simulated in the study,

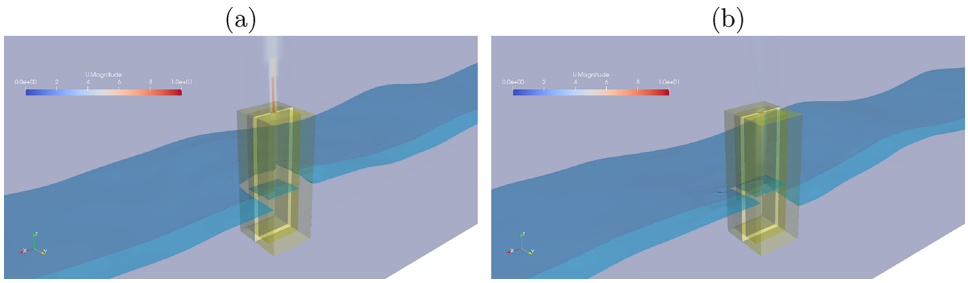

Fig. 11 Snapshots of the **a** exhale and **b** inhale of the two-way absorption simulations of RISE ($T = 0.82$ s and $H/\lambda = 0.025$)

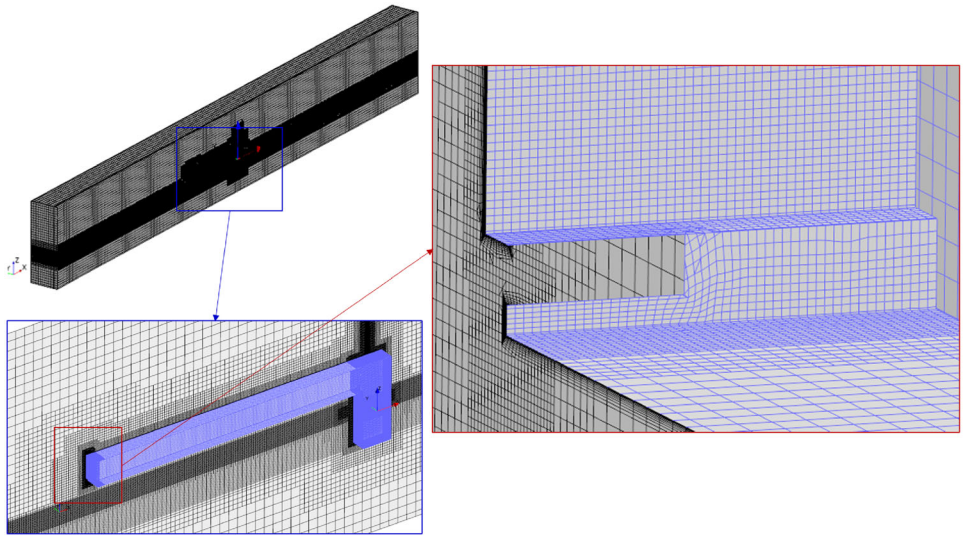

Fig. 12 The CFD mesh used in the NREL simulation with one-way absorption

resulting in a symmetric boundary condition for both lateral sides. A no-slip wall boundary condition was chosen for the bottom surface, whereas the top surface was defined as a pressure outlet condition. A trimmed cell mesh technique was used to generate a high-quality grid, particularly for the air-water interface as well as the regions surrounding the OWC body and its internal wave elevation regime. For of one-way absorption, the OWC's air chamber was extended to have an air volume equal to the experimental box and hose set up, a refinement volume was also generated. An example of mesh resolution for the one-wave absorption condition is graphically shown in Fig. 12. The total number of cells in the CFD model was approximately 4.57 million. To model the closing and opening valve condition in the one-way absorption cases, a set of cells was given a velocity source term that numerically specified zero velocity when the valve was closed and vice versa.

4.3 Overview of the numerical methods

Table 3 shows an overview of the methods applied by the potential flow teams. *Domain* with entries *FD* or *TD* denotes solutions in either the frequency domain or the time domain, respectively. *Coeffs* lists how the hydrodynamic coefficients were obtained with *Reference* denoting those described in Sect. 4.1. *Walls* refers to whether or not the flume walls have been included in the calculations. *DoF* denotes how many degrees of freedom were included for the chamber surface motions. *Turb. damp* describes whether the turbine damping model was linearized or not and *Visc. damp* shows whether or not a viscous damping model was included.

Table 4 gives an overview of the methods applied by the CFD teams.

4.4 Results

We first present results for the traditional two-way energy extraction, followed up by the novel one-way energy extraction (up- and down-stroke extraction). We include here results computed by the DTU frequency-domain and time-domain models, but note that these results were not part of the blind study. These two models are as described in Sect. 3.

4.4.1 Two-way absorption

For conventional two-way energy extraction, we present results for the internal chamber pressure and the non-dimensional absorbed power (CWR) of the double-chamber normalized by the chamber length $L = 7.5$ m at full scale.

Table 3 Overview of the potential flow methods

Team	Code	Domain	Coeffs	Walls	DoF	Turb. damp	Visc. damp
Ramboll	In-house	FD	Reference	Yes	One	Linear	No
DTU_{FD}	In-house	FD	Reference	Yes	Two	Linear	No
DTU_{TD}	DTUMotionSimulator	TD	Reference	Yes	Two	Nonlinear	No
Maynooth	In-house	TD	WAMIT	No	One	Nonlinear	No
MARIN	DIFFRAC	FD	DIFFRAC	No	One	Linear	Yes
NREL	WEC-Sim	TD	Reference	Yes	Two	Nonlinear	No

Table 4 Overview of the CFD methods

Team	Code	NSEq type	Turb. Model	Interface	Wave gen	Mean Δt	# of cells
SAGA	olaFlow	Incompres	None	VOF	Inlet BC	$7T/10{,}000$	0.35×10^6
RISE	interFOAM	Incompres	k-ω SST	VOF	Waves2FOAM	$\approx T/10{,}000$	2.7×10^6
NREL	StarCCM+	Compressible	k-ω SST	VOF	Inlet VOF BC	$T/400$	4.57×10^6

Pressure

For the presentation of the internal chamber pressure, we show the first harmonic amplitudes and compare the different numerical models adopted in the benchmark study. This value was computed by making a least-squares fit of the submitted time series to a sum of sines and cosines at the primary wave frequency plus four higher harmonics.

Figure 13a shows the non-dimensional chamber pressure as a function of model-scale wave period for the wave steepness $H/\lambda = 0.025$, whereas Fig. 13b shows the same for the wave steepness $H/\lambda = 0.04$. Consider first the potential flow models. With the exception of the MARIN model, they are all quite close to each other and mostly agree well with the experimental results. The results from the MARIN model are generally somewhat lower than the others, which is most likely due to the empirical viscous damping that is included in their model. The WEC-SIM and DTU-TD models are theoretically identical, and thus the small differences that appear here can be attributed to the different numerical implementations. The Maynooth model is also theoretically the same, but they consider the chamber in open water so the small differences here are attributed to the influence of the tank walls. Similarly, the DTU-FD and RAMBOLL results are very close, indicating that the influence of the sloshing mode is relatively small. There are also only small differences between the frequency-domain and time-domain results, which is consistent with the nearly linear wave conditions. Comparing the CFD results at the resonant period of $T = 0.82\,\mathrm{s}$ for the lower wave steepness, all three results agree very well and are towards the low end of the potential flow results. NREL and RISE results are also available at $T = 1.15\,\mathrm{s}$ and show a larger value than both experiments and potential flow calculations. The picture is very similar at the higher wave steepness value.

Figure 14a shows a representative period of the chamber pressure time history at the resonant period $T = 0.82\,\mathrm{s}$ for wave steepness $H/\lambda = 0.025$ and Fig. 14b shows the same for wave steepness $H/\lambda = 0.04$. For the DTU-FD method, the pressure has been computed from its purely linear definition, whereas in the RAMBOLL model the nonlinear equation (11) has been used, though the two choices give the same average absorbed power. All of the nonlinear models capture the quadratic behavior of the pressure around the zero crossing. Some larger variations in the peak amplitude and the phasing are evident from the time series, indicating some disagreement in terms of the higher harmonic components. With the exception of the MARIN model, the potential flow models predict a nearly symmetric behavior. However, the MARIN and CFD models, as well as the experiments, all show some asymmetry, though with a significant spread.

Absorbed power

The CWR from Eq. (16) (normalized by the length of the chamber $L = 0.15\,\mathrm{m}$ at model scale), is shown in Fig. 15a and b. A similar trend is seen here as for the pressure—the potential flow models are very close for most wave periods, except for the MARIN model which is generally somewhat lower. The experimental results are generally close to the potential flow values, though there is more spread near the resonant peak. The CFD models agree well with each other and with the experiments at $T = 0.82\,\mathrm{s}$ for both wave steepness values. At the lower steepness with at $T = 1.15\,\mathrm{s}$, the NREL-CFD and experimental results are very close but the RISE results are somewhat lower. For the higher steepness value in Fig. 15b, the NREL-CFD point at $T = 1.15\,\mathrm{s}$ also agrees well with the experiments, whereas the RISE result is somewhat lower. The NREL-CFD value at $T = 0.79\,\mathrm{s}$ is substantially lower than the experiments.

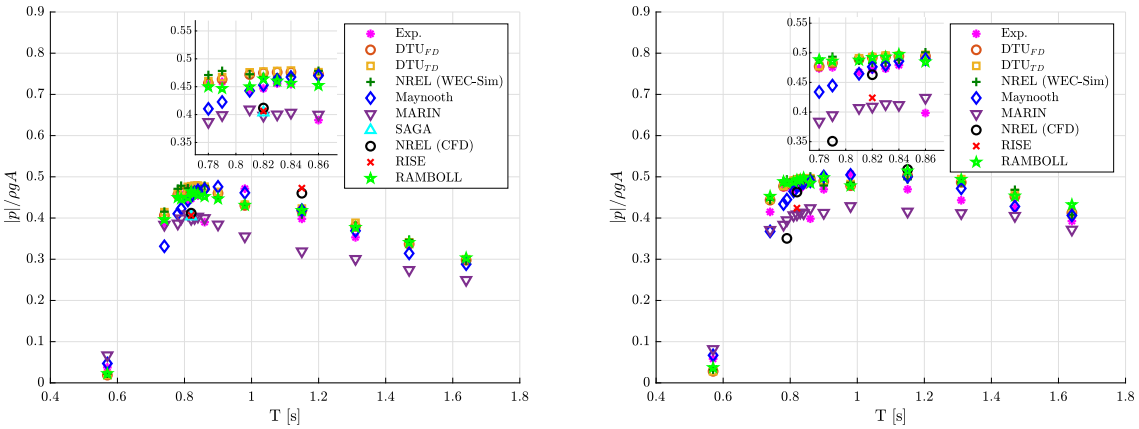

(a) $H/\lambda = 0.025$. (b) $H/\lambda = 0.04$.

Fig. 13 Non-dimensional chamber pressure, two-way absorption

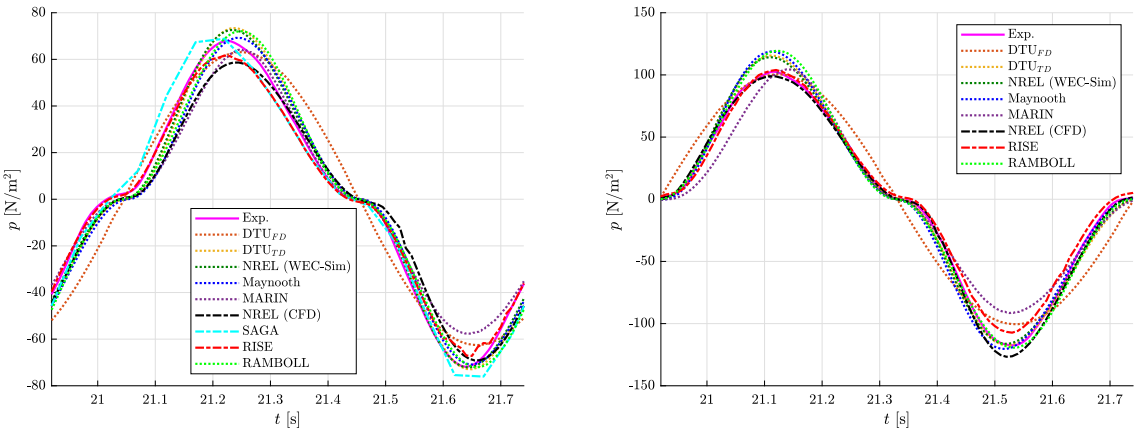

(a) $H/\lambda = 0.025$. (b) $H/\lambda = 0.04$.

Fig. 14 Chamber pressure at $T = 0.82$ s, two-way absorption

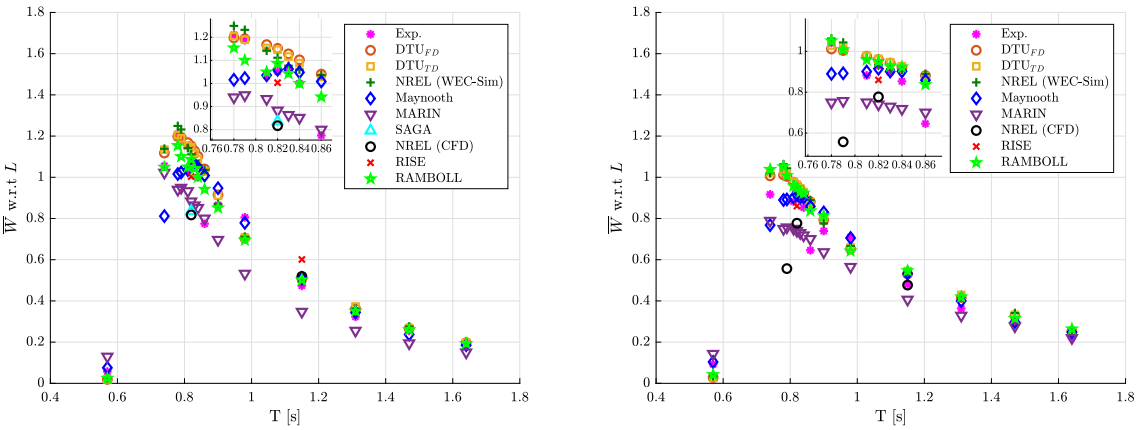

(a) $H/\lambda = 0.025$. (b) $H/\lambda = 0.04$.

Fig. 15 Capture width ratio, two-way absorption

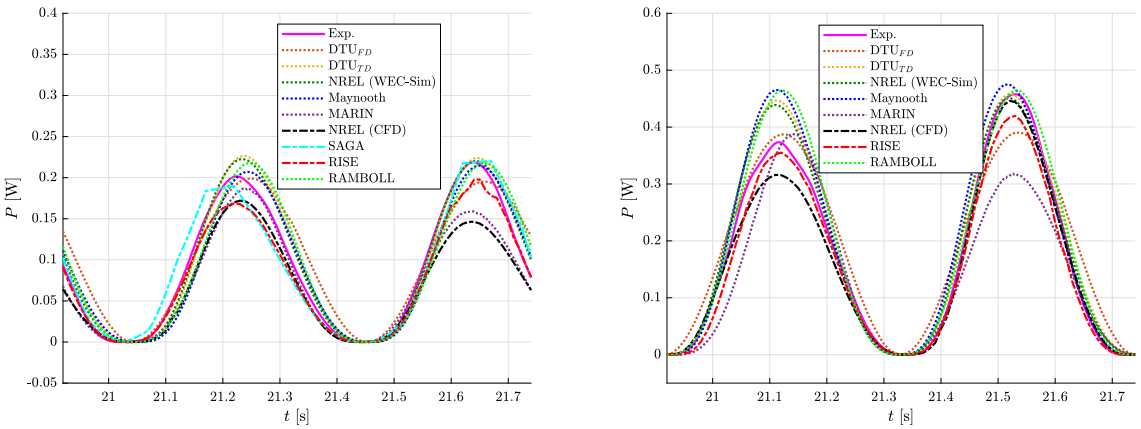

(a) $H/\lambda = 0.025$. (b) $H/\lambda = 0.04$.

Fig. 16 Absorbed power at $T = 0.82$ s, two-way absorption

Table 5 RMS differences. Two-way mean absorbed power, $H/\lambda = 0.025$

T	DTU$_{fd}$	DTU$_{td}$	NREL$_{WS}$	MARIN	Maynooth	Ramboll	NREL$_{CFD}$	RISE	SAGA
0.57	0.762	0.744	0.639	0.710	0.003	0.670			
0.74	0.022	0.036	0.040	0.073	0.246	0.035			
0.78	0.019	0.011	0.036	0.236	0.166	0.047			
0.79	0.009	0.005	0.050	0.201	0.131	0.067			
0.81	0.095	0.080	0.063	0.125	0.029	0.021			
0.82	0.073	0.070	0.026	0.174	0.008	0.016	0.224	0.135	0.279
0.83	0.064	0.055	0.023	0.181	0.001	0.010			
0.84	0.066	0.053	0.014	0.174	0.007	0.030			
0.86	0.364	0.345	0.364	0.040	0.326	0.228			
0.9	0.047	0.040	0.015	0.198	0.076	0.030			
0.98	0.130	0.126	0.131	0.347	0.025	0.130			
1.15	0.092	0.106	0.061	0.259	0.086	0.096	0.009	0.294	
1.31	0.206	0.232	0.205	0.139	0.118	0.179			
1.47	0.070	0.073	0.091	0.211	0.079	0.043			
1.64	0.122	0.168	0.102	0.481	0.021	0.035			

A representative period of the absorbed power time series for $T = 0.82$ s is shown in Fig. 16a and b. The figures show trends similar to those for the pressure. As expected, the NREL-WEC-Sim and DTU-TD models are nearly identical, with the RAMBOLL results also close, the DTU-FD results are strictly linear and the MARIN results are somewhat lower and asymmetric. For the low steepness case, the experiments, the CFD results and the MARIN model all predict a higher power peak on the up-stroke compared to the down-stroke, whereas for the higher wave steepness case they find the reverse. It is not clear what causes this, but it may be associated with an asymmetry in the vortex generation between the two cycles. The other potential flow models do not find any significant difference between absorption on the up-stroke and down-stroke. The experimental results show some high-frequency content that is not found by the numerical calculations.

To provide a more quantitative measure of the differences between the calculations and the measurements, Table 5 collects the normalized root mean square errors (RMSE) in the mean absorbed power for each team in the case $\epsilon = 0.025$. This is computed from

$$\text{RMSE} = \frac{1}{\overline{P}_e}\sqrt{(\overline{P}_e - \overline{P}_c)^2} \tag{22}$$

where the subscripts e and c indicate the experimental and computed values, respectively.

4.4.2 Up-stroke absorption

For the up-stroke absorption strategy, power is only extracted from the OWC chamber as the internal surface moves from trough to crest. Figure 17a and b shows a representative wave

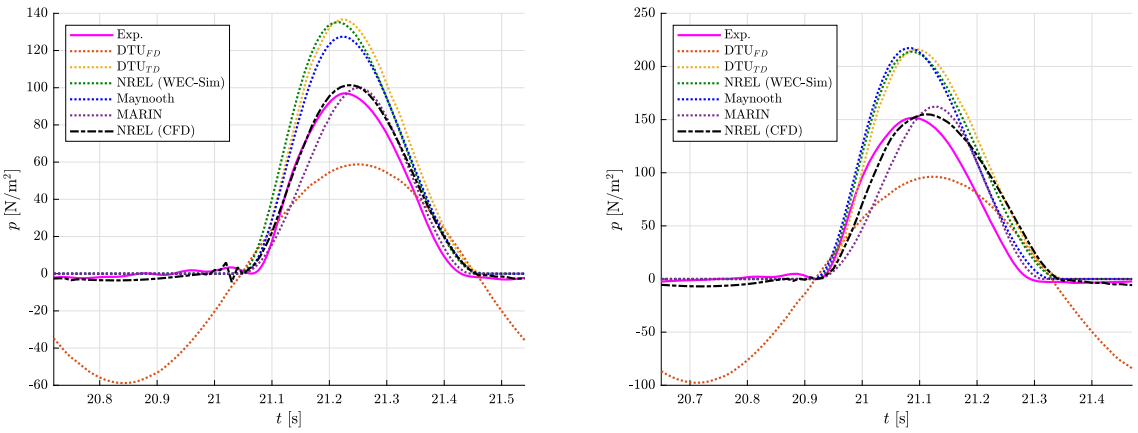

(a) $H/\lambda = 0.025$. (b) $H/\lambda = 0.04$.

Fig. 17 Chamber pressure for $T = 0.82$ s, up-stroke absorption

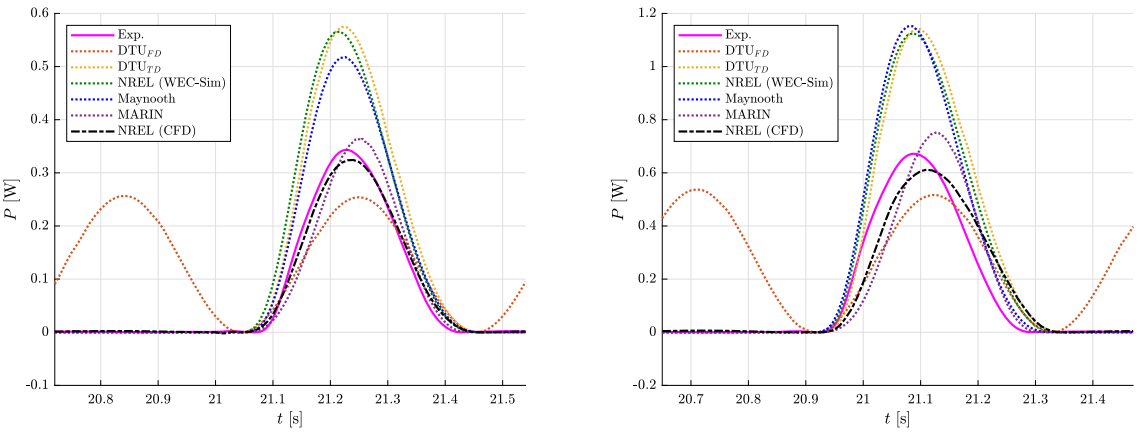

(a) $H/\lambda = 0.025$. (b) $H/\lambda = 0.04$.

Fig. 18 Absorbed power at $T = 0.82$ s, up-stroke absorption

period of the time series of chamber pressure for $T = 0.82$ s. Here it is clear that the various venting models (experimental and numerical) more or less ensure that the pressure inside the chamber is zero (atmospheric) during the down-stroke and positive, while energy is extracted on the up-stroke. The exception is, of course, the strictly linear DTU-FD model which must retain a sinusoidal pressure variation. Looking closely at the experimental and the CFD results during the passive cycle, however, it is clear that there is a significant non-zero pressure inside the chamber suggesting that there is some flow through the orifice with an associated energy loss. A delay in the increase of pressure is also clear in these curves when the valve is supposed to close, suggesting additional energy loss compared to the ideal situation. Figure 18a and b shows the corresponding time series of absorbed power. Figure 19a and b shows the CWR of the chamber for the up-stroke absorption strategy as a function of the wave period. Here, we again see a very good agreement between the NREL-WEC-Sim and DTU-TD results, with some small differences compared to the DTU-FD calculations. These predictions are consistently much larger than the experimental values. The Maynooth results show a somewhat lower and slightly shifted peak, whereas the MARIN results are substantially lower and generally closer to the experimental results. The NREL-CFD results at $T = 0.82$ s agree well with the experiments. The RMS differences between the measurements and the calculations are collected in Table 6 for the 0.025 steepness case as a quantitative comparison.

4.4.3 Down-stroke absorption

For the down-stroke absorption strategy, power is only extracted as the internal chamber surface moves from peak to trough. Figure 20a and b shows a representative period of the chamber pressure time series for the case of $T = 0.82$ s. Figure 21a and b shows the corresponding time series of absorbed power.

Figure 22a and b shows the CWR of the chamber for the down-stroke absorption strategy as a function of the wave period. The trends here are very similar to that seen for the up-

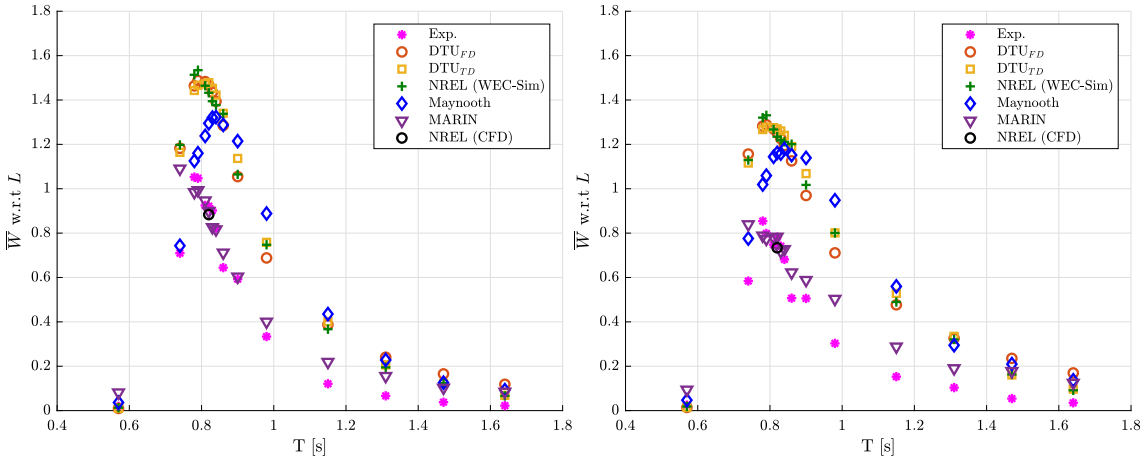

(a) $H/\lambda = 0.025$. (b) $H/\lambda = 0.04$.

Fig. 19 Capture width ratio, up-stroke absorption

Table 6 RMS differences. Up-stroke mean absorbed power, $H/\lambda = 0.025$

T	DTU$_{fd}$	DTU$_{td}$	NREL$_{WS}$	MARIN	Maynooth	NREL$_{CFD}$
0.57	0.563	0.572	0.425	2.785	0.988	
0.74	0.693	0.660	0.715	0.536	0.121	
0.78	0.394	0.373	0.438	0.078	0.087	
0.79	0.456	0.436	0.502	0.034	0.165	
0.81	0.635	0.620	0.611	0.035	0.389	
0.82	0.605	0.620	0.570	0.007	0.443	0.034
0.83	0.627	0.648	0.583	0.069	0.513	
0.84	0.676	0.712	0.658	0.015	0.597	
0.86	1.029	1.115	1.110	0.089	1.057	
0.9	0.760	0.895	0.774	0.033	1.002	
0.98	1.013	1.221	1.190	0.161	1.625	
1.15	2.435	2.573	2.271	0.924	2.435	
1.31	2.471	1.962	1.805	1.288	1.746	
1.47	2.961	1.887	1.853	1.490	1.510	
1.64	11.203	5.927	5.725	5.761	6.692	

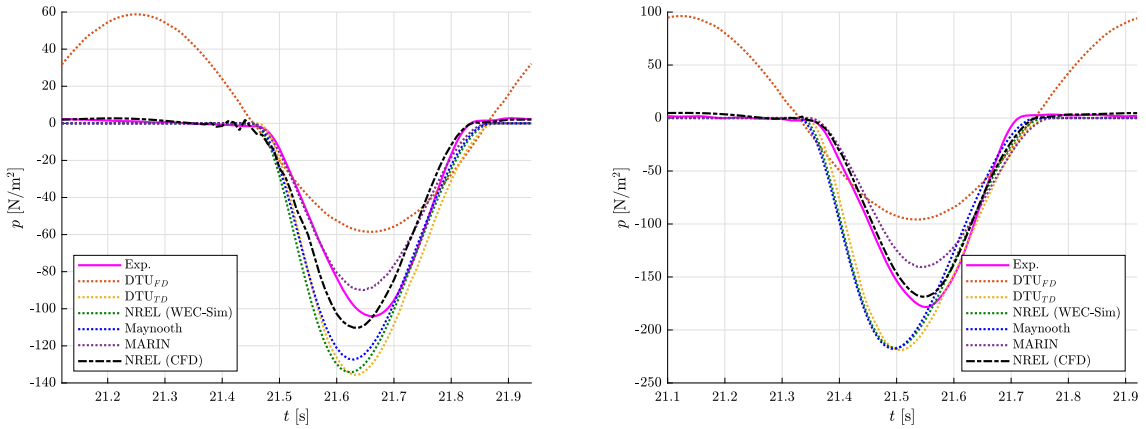

(a) $H/\lambda = 0.025$. (b) $H/\lambda = 0.04$.

Fig. 20 Chamber pressure for $T = 0.82$ s, down-stroke absorption

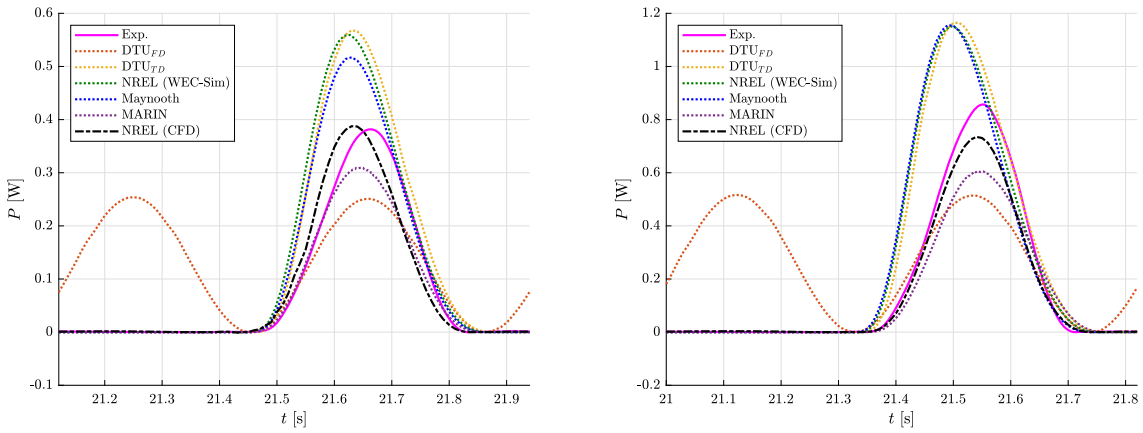

(a) $H/\lambda = 0.025$. (b) $H/\lambda = 0.04$.

Fig. 21 Absorbed power for $T = 0.82$ s, down-stroke absorption

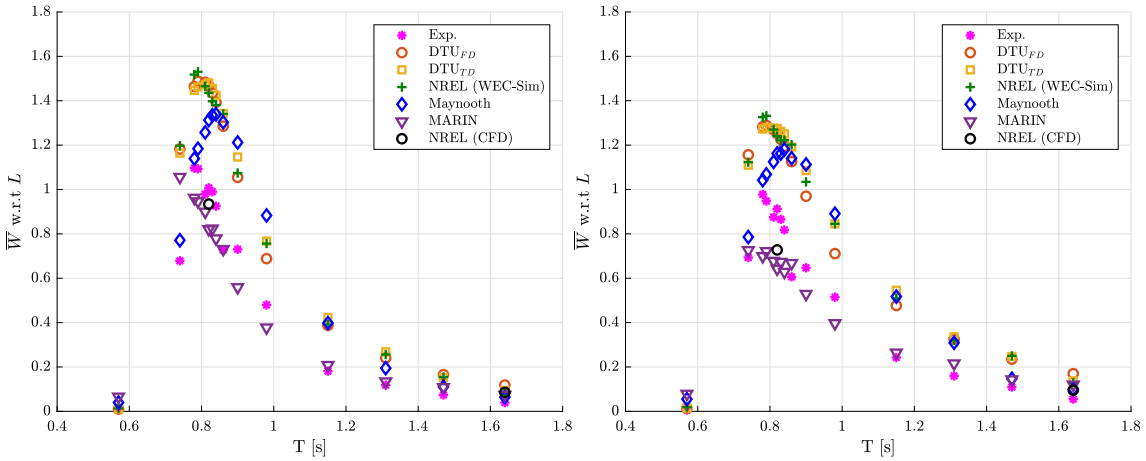

(a) $H/\lambda = 0.025$. (b) $H/\lambda = 0.04$.

Fig. 22 Capture width ratio, down-stroke absorption

stroke absorption case. Table 7 collects the RMS differences between the calculations and the measurements for the 0.025 steepness case.

5 Discussion

For two-way absorption, the measured and computed pressures and CWR generally agree quite well. Although we have not carefully estimated a confidence bound for the experimental uncertainties in these measurements, the calculations are mostly within what we expect those bounds to be. The exception is the MARIN results which are substantially lower than the others, presumably because the viscous damping has been over-estimated in this model. For one-way absorption, however, we find a much larger spread in the numerical predictions which generally show a much larger energy absorption than the measurements. It is clear from the measurements that the passive one-way valve system used for these experiments allowed for significant energy loss on the passive cycle, which we suspect explains a large part of the discrepancy, but this must be confirmed by new measurements using a better release valve system. The MARIN results here are generally close to the experiments, indicating that the choice of viscous damping captures a similar overall energy loss. The two CFD results at the natural period also agree well with the experiments, but it is worth mentioning that modeling the release valve in these calculations was also challenging and some energy loss on the passive cycle is also clear in the associated time series of pressure. The rest of the potential flow calculations agree relatively well with each other, though the influence of the channel walls is more pronounced here than it was in the two-way case.

This seemingly simple test case clearly holds many challenges for both numerical analysis and experimental measurement. We note that the collapse of the calculations to what is shown here in this paper did not happen immediately at the close of the benchmark study. In the first round

Table 7 RMS differences. Down-stroke mean absorbed power, $H/\lambda = 0.025$

T	DTU_{fd}	DTU_{td}	NREL_{WS}	MARIN	Maynooth	NREL_{CFD}
0.57	0.545	0.437	0.271	2.208	0.649	
0.74	0.726	0.700	0.754	0.536	0.099	
0.78	0.352	0.340	0.405	0.109	0.044	
0.79	0.383	0.362	0.422	0.122	0.081	
0.81	0.517	0.506	0.498	0.073	0.263	
0.82	0.478	0.492	0.447	0.175	0.305	0.067
0.83	0.476	0.500	0.441	0.137	0.357	
0.84	0.463	0.495	0.450	0.180	0.381	
0.86	0.797	0.870	0.867	0.031	0.796	
0.9	0.462	0.588	0.489	0.238	0.678	
0.98	0.405	0.561	0.540	0.234	0.854	
1.15	1.042	1.195	1.027	0.088	1.280	
1.31	0.914	1.099	1.003	0.077	0.736	
1.47	1.101	0.957	0.957	0.384	0.565	
1.64	5.557	3.880	3.559	2.160	4.981	0.534

of comparisons, the spread was dramatic, which allowed the teams to identify minor bugs and inconsistencies in their calculations and arrive at the final consensus. This is a good lesson that even seemingly simple cases can be prone to simple errors, highlighting the benefit of comparing independent calculations of the same case.

6 Conclusions

We have presented the results of a benchmark study for a single fixed OWC chamber in regular waves of two steepness values, comparing measured and computed response for both two-way and one-way energy absorption strategies. The results highlight the challenges associated with this seemingly simple device, especially with the one-way absorption strategy which is difficult to perfectly implement both physically and numerically. Potential flow calculations predict that as much, or in some cases more, energy can be absorbed using the one-way strategy, but the opposite is shown by the measurements and CFD calculations. However, a better physical release valve system is required to confirm this one way or the other. A better release valve model in the CFD calculations should also be developed and more calculations performed to illuminate the physics of the one-way response.

Acknowledgements The Danish participants would like to thank the Danish Energy Technology Development and Demonstration Program (EUDP) grant number 64020-1105 for supporting this work. The Swedish participants were supported by the Swedish Energy Agency under grant no 44423-2. The Irish participants would like to acknowledge the support of Science Foundation Ireland (SFI) through the MaREI Centre for Energy, Climate and Marine under Grant No. 12/RC/2302_P2. The Japanese participants were supported by the computer resource offered under the category of General Projects by the Research Institute for Information Technology, Kyushu University. This work was authored in part by the National Renewable Energy Laboratory, operated by Alliance for Sustainable Energy, LLC, for the U.S. Department of Energy (DOE) under Contract No. DE-AC36-08GO28308. Funding provided by U.S. Department of Energy Office of Energy Efficiency and Renewable Energy Water Power Technologies Office. The views expressed in the article do not necessarily represent the views of the DOE or the U.S. Government. The U.S. Government retains and the publisher, by accepting the article for publication, acknowledges that the U.S. Government retains a nonexclusive, paid-up, irrevocable, worldwide license to publish or reproduce the published form of this work, or allow others to do so, for U.S. Government purposes.

Author Contributions H.B.B. wrote the main manuscript text, and B.J. collected and processed the data and prepared the main figures. All the authors made calculations and engaged in discussions during the study and preparation of the manuscript. All the authors prepared figures and text describing their numerical models. All the authors reviewed the manuscript.

Funding Open access funding provided by Technical University of Denmark See Acknowledgements.

Data availability On request.

Code Availability DTUMotionSimulator and Wec-Sim are available open source, see references.

Declarations

Conflict of interest None.

Ethics approval and consent to participate Not applicable.

Consent for publication Given.

Materials availability Not applicable.

References

Batchelor GK (1967) An introduction to fluid dynamics. Cambridge University Press, Cambridge

Bingham HB, Read R (2023) DTUMotionSimulator; a Matlab package for simulating linear or weakly nonlinear response of a floating structure to ocean waves. https://gitlab.gbar.dtu.dk/oceanwave3d/DTUMotionSimulator

Bingham HB, Ducasse D, Nielsen K et al (2015) Hydrodynamic analysis of oscillating water column, wave energy devices. J Ocean Eng Mar Energy 1(4):405–419

Bingham HB, Yu YH, Nielsen K et al (2021) Ocean energy systems wave energy modelling task 10.4: numerical modelling of a fixed oscillating water column. Energies 14:1718. https://doi.org/10.3390/en14061718

Cruz J (2008) Ocean wave energy. Current status and future perspectives. Springer, Berlin

Cummins WE (1962) The impulse response function and ship motions. Schiffstecknik 9:101–109

Drew B, Plummer AR, Sahinkaya M (2009) A review of wave energy converter technology. Proc Inst Mech Eng Part A J Power Energy 223:887–902

Eça L, Hoekstra M (2014) A procedure for the estimation of the numerical uncertainty of CFD calculations based on grid refinement studies. J Comput Phys 262:104–130

Falcão AFO (2010) Wave energy utilization: a review of the technologies. Renew Sustain Energy Rev 14:899–918

Falcão AF, Henriques JC (2016) Oscillating-water-column wave energy converters and air turbines: a review. Renew Energy 85:1391–1424

Falnes J (2002) Ocean waves and oscillating systems. Cambridge University Press, Cambridge

Guo Y, Yu YH, van Rij J, et al (2017) Inclusion of structural flexibility in design load analysis for wave energy converters. In: 12th European Wave and Tidal Energy Conference. EWTEC

Guo B, Patton RJ, Jin S et al (2018) Numerical and experimental studies of excitation force approximation for wave energy conversion. Renew Energy 125:877–889

Heath T (2012) A review of oscillating water columns. Philos Trans R Soc Lond A 370:235–245

Higuera P (2017) olaFlow: CFD for waves Software. https://doi.org/10.5281/zenodo.1297013. https://olaflow.github.io

Higuera P, Lara JL, Losada IJ (2013) Realistic wave generation and active wave absorption for Navier–Stokes models: application to OpenFOAM®. Coast Eng 71:102–118. https://doi.org/10.1016/j.coastaleng.2012.07.002

Higuera P, Lara J, Losada I (2015) Three-dimensional numerical wave generation with moving boundaries. Coast Eng 101:35–47. https://doi.org/10.1016/j.coastaleng.2015.04.003

IEA (2022) OES-Ocean Energy Systems, an International Energy Agency Technology Initiative. http://www.ocean-energy-systems.org

Jacobsen N, Fuhrman D, Fredsoe J (2012) A wave generation toolbox for the open-source CFD-library OpenFOAM. Int J Numer Methods Fluids 70:1073–1088

Joensen B, Bingham HB, Read RW, et al (2021) Performance predictions of one-way energy capture by an oscillating water column device in faroese waters. In: Proceedings of the 14th European wave and tidal energy conference. EWTEC, Plymouth, UK, 5-9, Sept,, pp 1–6

Joensen B, Bingham HB, Read RW et al (2023) Hydrodynamic analysis of one-way energy capture by an oscillating water column wave energy device. Energy Rep 9:5306–5322. https://doi.org/10.1016/j.egyr.2023.04.052

Kramer M, Andersen J, Thomas S et al (2021) Highly accurate experimental heave decay tests with a floating sphere: a publich benchmark dataset for model validation of fluid-structure interaction. Energies 14:269. https://doi.org/10.3390/en14020269

Liu C, Huang Z, Law Wing Keung A, et al (2010) A numerical study of wave energy converter in the form of an oscillating water column based on a mixed Eulerian–Lagrangian formulation. In: International conference on offshore mechanics and arctic engineering. OMAE, June 6–11, Shanghai, China, pp 589–596

MARIN (2022) Theory documentation DIFFRAC-v3.5.0. https://www.marin.nl/en/facilities-and-tools/software/diffrac. Accessed Feb 2025

McCormick M (2007) Ocean wave energy conversion. Dover, Mineola

Menter F, Kuntz M, Langtry R (2003) Ten years of industrial experience with the SST turbulence model. In: Proceedings of the 4th International Symposium on Turbulence, Heat and Mass Transfer. Begell House, Antalya, Turkey, pp 625–632

Newman JN (1994) Wave effects on deformable bodies. Appl Ocean Res 16(1):47–59

Newman JN (2017) Marine Hydrodynamics-40th Anniversary Edition. The MIT Press, Cambridge. open Access e-book available from https://mitpress.mit.edu/books/marine-hydrodynamics-40th-anniversary-edition

Newman JN, Lee CH (2023) WAMIT; a radiation-diffraction panel program for wave-body interactions. http://www.wamit.com. Accessed Feb 2025

OpenCFD (2023) OpenFOAM (open source field operation and manipulation). http://www.openfoam.com. Accessed Feb 2025

Opoku F, Uddin M, Atkinson M (2023) A review of computational methods for studying oscillating water columns-the Navier–Stokes based equation approach. Renew Sustain Energy Rev 174:113124

Pauw WH, Huijsmans RH, Voogt A (2007) Advances in the hydrodynamics of side-by-side moored vessels. In: International conference on offshore mechanics and arctic engineering. ISOPE, Lisbon, Portugal, July 1–6, pp 597–603

Pena-Sanchez Y, Faedo N, Penalba M, et al (2019) Finite-order hydrodynamic approximation by moment-matching (FOAMM) toolbox for wave energy applications. In: Proceedings of European tidal and wave energy conference. EWTEC, Naples

Rosati M, Henriques J, Ringwood J (2022) Oscillating-water-column wave energy converters: a critical review of numerical modelling and control. Energy Convers Manag X 16:100322

Trevino JB (2020) Experimental investigation of one-way energy capture by an OWC wave energy device. Master's thesis, Technical University of Denmark, Department of Mechanical Engineering

WEC-Sim Development Team (2023) WEC-Sim (Wave Energy Converter SIMulator). https://wec-sim.github.io/WEC-Sim/. Accessed Feb 2025

Weller H, Tabor G, Jasak H et al (1998) A tensorial approach to CFD using object oriented techniques. Comput Phys 12:620–631

Wendt F, Nielsen K, Yu YH et al (2019) Ocean energy systems wave energy modelling task: modelling, verification and validation of wave energy converters. J Mar Sci Eng 7:22

Yu YH, Lawson M, Ruehl K, et al (2014) Development and demonstration of the WEC-Sim wave energy converter simulation tool. METS

Zabala I, Henriques J, Blanco J et al (2019) Wave-induced real-fluid effects in marine energy converters: review and application to owc devices. Renew Sustain Energy Rev 111:535–549

Zhao M, Ning D (2024) A review of numerical methods for studying hydrodynamic performance of oscillating water column (owc) devices. Renew Energy 233:121177

Authors and Affiliations

Harry B. Bingham[1] · Bárður Joensen[1,2] · Robert W. Read[1] · Kim Nielsen[3,4] · Thanh Toan Tran[5] · Hafiz Ahsan Said[6] · Thomas Kelly[7] · John V. Ringwood[6] · Yasutaka Imai[8] · Joep van der Zanden[9] · Yi-Hsiang Yu[10] · Claes Eskilsson[4,11] · Alex Abolfazl Shiri[11]

✉ Harry B. Bingham
hbbi@dtu.dk

Bárður Joensen
bardurj@setur.fo

Robert W. Read
rrea@dtu.dk

Kim Nielsen
kimnielsenoceanenergy@gmail.com

Thanh Toan Tran
ThanhToan.Tran@nrel.gov

Hafiz Ahsan Said
hafiz.said.2020@mumail.ie

Thomas Kelly
kellyt@dkit.ie

John V. Ringwood
john.ringwood@mu.ie

Yasutaka Imai
imaiy@cc.saga-u.ac.jp

Joep van der Zanden
j.v.d.zanden@marin.nl

Yi-Hsiang Yu
yyu@nycu.edu.tw

Claes Eskilsson
claese@build.aau.dk

Alex Abolfazl Shiri
alex.shiri@ri.se

[1] Department of Civil and Mechanical Engineering, Technical University of Denmark (DTU), Nils Koppels Allé, 2800 Lyngby, Denmark

[2] Department of Science and Technology, University of the Faroe Islands, Vestara Bryggja 15, FO-110 Tórshavn, Faroe Islands, Denmark

[3] Ramboll Group A/S, Hannemanns Allé 53, 2300 Copenhagen, Denmark

[4] Department of the Built Environment, Aalborg University (AAU), Thomas Mann Vej 23, 9220 Aalborg Ø, Denmark

[5] National Renewable Energy Laboratory (NREL), 15013 Denver West Parkway, Golden, CO 80401, USA

[6] Centre for Ocean Energy Research, Maynooth University (MU), Maynooth, Co. Kildare W23 F2H6, Ireland

[7] Centre for Renewable Energy at Dundalk IT, Dundalk IT, Dundalk, Co. Louth A91 K584, Ireland

[8] Institute of Ocean Energy, Saga University (SAGA), Saga 8408502, Japan

[9] Offshore Department, Maritime Research Institute Netherlands (MARIN), Haagsteeg 2, Wageningen 6708 PM, The Netherlands

[10] Department of Civil Engineering, National Yang Ming Chiao Tung University, Hsinchu City 30010, Taiwan

[11] Maritime Department, Research Institutes of Sweden (RISE), 412 58 Göteborg, Sweden